IOP Publishing Phys. Med. Biol. 69 (2024) 085027 https://doi.org/10.1088/1361-6560/ad33b6

Physics in Medicine & Biology

IPEM Institute of Physics and Engineering in Medicine

OPEN ACCESS

RECEIVED
6 November 2023

REVISED
20 February 2024

ACCEPTED FOR PUBLICATION
13 March 2024

PUBLISHED
9 April 2024

PAPER

3D whole heart k-space-based super-resolution cardiac T1 mapping using rotated stacks

Simone Hufnagel[1], **Patrick Schuenke**[1], **Jeanette Schulz-Menger**[2,3,4], **Tobias Schaeffter**[1,5,6] and **Christoph Kolbitsch**[1]

[1] Physikalisch-Technische Bundesanstalt (PTB), Braunschweig and Berlin, Germany
[2] Charité Medical Faculty University Medicine, Berlin, Germany
[3] Working Group on Cardiovascular Magnetic Resonance, Experimental and Clinical Research Center (ECRC), Charité Humboldt University Berlin, DZHK partner site Berlin, Berlin, Germany
[4] Department of Cardiology and Nephrology, HELIOS Klinikum Berlin Buch, Berlin, Germany
[5] Department of Biomedical Engineering, Technical University of Berlin, Berlin, Germany
[6] Einstein Center Digital Future, Berlin, Germany

E-mail: simone.hufnagel@ptb.de

Keywords: super-resolution, T_1 mapping, k-space-based reconstruction, cardiovascular MR, myocardial tissue characterization, whole-heart, 3D

Abstract

Objective. To provide three-dimensional (3D) whole-heart high-resolution isotropic cardiac T1 maps using a k-space-based through-plane super-resolution reconstruction (SRR) with rotated multi-slice stacks. *Approach*. Due to limited SNR and cardiac motion, often only 2D T1 maps with low through-plane resolution (4–8 mm) can be obtained. Previous approaches used SRR to calculate 3D high-resolution isotropic cardiac T1 maps. However, they were limited to the ventricles. The proposed approach acquires rotated stacks in long-axis orientation with high in-plane resolution but low through-plane resolution. This results in radially overlapping stacks from which high-resolution T1 maps of the whole heart are reconstructed using a k-space-based SRR framework considering the complete acquisition model. Cardiac and residual respiratory motion between different breath holds is estimated and incorporated into the reconstruction. The proposed approach was evaluated in simulations and phantom experiments and successfully applied to ten healthy subjects.*Main results*. 3D T1 maps of the whole heart were obtained in the same acquisition time as previous methods covering only the ventricles. T1 measurements were possible even for small structures, such as the atrial wall. The proposed approach provided accurate ($P > 0.4$; $R^2 > 0.99$) and precise T1 values (SD of 64.32 ± 22.77 ms in the proposed approach, 44.73 ± 31.9 ms in the reference). The edge sharpness of the T1 maps was increased by 6.20% and 4.73% in simulation and phantom experiments, respectively. Contrast-to-noise ratios between the septum and blood pool increased by 14.50% in *in vivo* measurements with a k-space compared to an image-space-based SRR. *Significance*. The proposed approach provided whole-heart high-resolution 1.3 mm isotropic T1 maps in an overall acquisition time of approximately three minutes. Small structures, such as the atrial and right ventricular walls, could be visualized in the T1 maps.

1. Introduction

Cardiac T1 mapping provides valuable quantitative information for the diagnosis of a variety of heart diseases (Schelbert and Messroghli 2016, Haaf *et al* 2017, Al-Wakeel-Marquard *et al* 2021). While in clinical routine diagnostics are more focused on the left ventricle, quantitative imaging of the right ventricular wall (Asano *et al* 2021) or the atrial wall (Beinart *et al* 2013) is also of high diagnostic value. Isotropic high-resolution whole-heart coverage would strongly improve diagnostic information about fibrosis in atrial walls in arrhythmic patients (Beinart *et al* 2013) and improve diagnostic capability in patients with pulmonary arterial hypertension (Asano

et al 2021). As these structures are usually very thin (Whitaker *et al* 2016) (between 1 and 4 mm) and complexly curved, high spatial resolution is needed. However, especially image resolution along the slice-encoding (SE) direction is often restricted due to limited acquisition time or signal-to-noise ratio (SNR) limitations.

Super-resolution reconstruction (SRR) has been shown to improve the trade-off between acquisition time, SNR, and spatial through-plane resolution (Plenge *et al* 2012a). For that, several multi-slice stacks with high in-plane but low resolution (LR) along the SE direction are acquired, providing overlapping stacks of the object, from which a high-resolution (HR) volume is reconstructed. In quantitative imaging, model-based SRR incorporates the knowledge about the signal model (for example T1 relaxation) and data acquisition model into the optimization. Commonly (Van Steenkiste *et al* 2016, Van Steenkiste *et al* 2017, Beirinckx *et al* 2020, 2022, Hufnagel *et al* 2022), image-space-based SRR is used, where the LR images are reconstructed in an initial step, then serve as a starting point for the SRR and the difference between the acquired LR dynamics and those predicted from the SRR result is minimized. Others (Bano *et al* 2020, Corona *et al* 2021) used a k-space-based SRR approach, minimising the difference between the acquired k-space data and the one predicted from the SRR result. Thereby the coil sensitivity maps and Fourier transformation (FT) were integrated into the optimization, which improved the visualization of small structures compared to an image-space-based reconstruction. Nevertheless, k-space-based SRR has so far only been applied to qualitative imaging (Corona *et al* 2021) or quantitative cartesian brain imaging (Bano *et al* 2020). In addition to limited spatial resolution, the coverage of the entire heart is another challenge for cardiac SRR. Previous image-space-based cardiac T1 mapping SRR methods (Hufnagel *et al* 2022) used LR stacks in short-axis orientation (SAX), which were shifted to each other to improve resolution along the SE direction but could only cover the ventricles. So far, whole-heart T1 mapping with high isotropic resolution (below or equal to 1.5 mm) is only possible with long acquisition times (>9 min) (Milotta *et al* 2020, Nordio *et al* 2020, Qi *et al* 2019a, 2020, Qi *et al* 2019b, 2022, Phair *et al* 2023).

In this paper, a new k-space-based SRR approach is presented to overcome both challenges by acquiring rotated stacks, rotating from the four-chamber orientation (4CH) over the two-chamber orientation (2CH) by using the septum as the rotation axis. This is similar to a previously presented cine magnetic resonance imaging (MRI) approach using slices at differently rotated long-axis orientations for obtaining volumetric data (Bloomer *et al* 2001) but using a different rotation axis. This acquisition mode ensures that the stacks overlap and provide information about the complete heart, especially along the LR SE direction. The proposed SRR approach is model-based and considers the T1-relaxation signal model in the SRR framework. Cardiac and residual respiratory motion displacements are estimated and incorporated into the reconstruction. Furthermore, the presented approach is k-space-based to enable T1 mapping of even thin structures such as the atrial wall. For this, the breath hold (BH) motion information, the cardiac motion information, the slice profile, the coil sensitivity maps, the radial k-space trajectory, and the FT are incorporated into a common SRR framework.

The proposed approach was evaluated in numerical simulations by comparing the proposed k-space-based SRR approach with an image-space-based SRR approach and with a previously published (Hufnagel *et al* 2022) SRR approach using shifted slices in SAX orientation. Furthermore, the proposed approach was tested in phantom experiments and its *in vivo* applicability was demonstrated in ten healthy subjects by obtaining T1-maps of the whole heart with an isotropic resolution of 1.3 mm in approximately three minutes of total acquisition time.

2. Methods

The proposed workflow to acquire whole-heart isotropic T1 maps using k-space-based SRR is depicted in figure 1. Multiple stacks of two-dimensional (2D) slices with high in-plane but low through-plane resolution are acquired at different angles using a SRR acquisition scheme with rotated stacks with one stack per BH. This results in radially overlapping stacks covering the whole heart. The respective k-space data is then used to reconstruct LR dynamics and T1 maps, which are needed to estimate cardiac and BH alignment motion. The proposed scheme is k-space-based, so the SRR is applied to the raw k-space data and, therefore, also includes information about the k-space trajectory R, the coil maps C and the Fourier transform F. Data consistency was ensured between the acquired k-space data and the k-space data resulting from the application of the acquisition model on the SRR result. After the iterative optimization scheme of the SRR, a HR three-dimensional (3D) T1 map is obtained.

2.1. K-space-based SRR

For the proposed k-space-based SRR, the difference between the acquired k-space data y and the k-space data predicted from applying the acquisition model on the SRR volume is minimized (see equation (4)).

The acquisition model thereby consists of the T1 relaxation model q, translational BH motion M^B, downsampling operator A, cardiac motion fields M^C, coil maps C, Fourier transform F, and the radial k-space

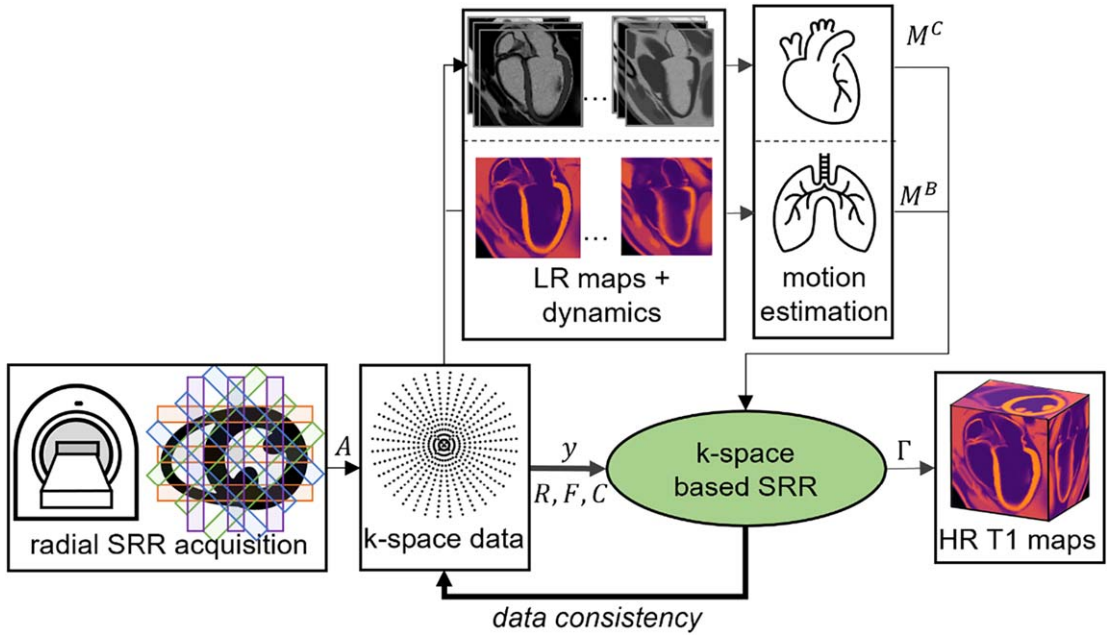

Figure 1. Schematic pipeline of the proposed approach. The data was acquired using multiple receiver coils and a Golden radial k-space trajectory. Several stacks were acquired with long-axis orientations rotated to each other (A). This results in radially overlapping stacks with high in-plane but low through-plane resolution. Before data acquisition, multiple inversion pulses were applied to make the sequence T1 sensitive. For cardiac and BH motion estimation, LR dynamics and T1 maps were reconstructed in an initial step and the estimated motion M^C and M^B were input for the following SRR. The SRR was k-space-based, so the acquired k-space data y as well as the radial k-space trajectory R, coil maps C, Fourier transform F, and T1 relaxation model were part of the acquisition model. The motion fields ensure that the output of the reconstruction is a motion-corrected HR 3D T1 map Γ reconstructed from k-space data from different motion states.

sampling operator R. Corresponding to the Look–Locker Model (Look and Locker 1970), q describes a three-parameter (M_0, α, T_1) signal behaviour (Deichmann and Haase 1992) for all t_i ($i = 0,\ldots,N_i$ and N_i being the number of reconstructed inversion times) of the continuous data acquisition after the inversion pulse, with α describing the flip angle of the read-out pulses, and M_0 the equilibrium magnetisation:

$$q(M_0,\ \alpha,\ T_1) = M_0^* - (M_0 + M_0^*)\exp\left(-\frac{t_i}{T_1^*}\right) \tag{1}$$

$$M_0^* = \frac{M_0 \quad T_1^*}{T_1} \tag{2}$$

$$T_1^* = \left[\frac{1}{T_1} - \left(\frac{1}{\mathrm{TR}}\right)\ln(\cos(\alpha))\right]^{-1}, \tag{3}$$

TR thereby describes the repetition time. The calculation of M^B and M^C is further explained in sub-section 2.3. The used Fourier transform was non-uniform (Jackson *et al* 1991, Keiner *et al* 2009).

For regularization, the parameter k weights the influence of the total variation regularization based on the forward finite differences operator G and the data consistency term. The sum over all stacks s and inversion times t (with $s = 1,\ldots N_S$ and $t = 1,\ldots,N_T$, with N_S being the number of stacks and N_T being the number of inversion times) is minimized:

$$\min_{\Gamma} \sum_{s=1}^{N_S}\sum_{t=1}^{N_T} ||y_{t,s} - R\ F\ C_s\ M_{t,s}^C\ M_s^B\ A_s\ q_t(\Gamma)||_2^2 + k\ ||G\ \Gamma||_1. \tag{4}$$

As the LR stacks are rotated around the phase-encoding (PE) axis, shifts in the PE direction correspond to a shift in the in-plane dimension of the LR images. Therefore, M^B only includes the readout and SE direction of the detected motion, while the translation in the PE direction is implemented as a preprocessing phase shift directly applied to the acquired k-space data.

Since the non-smoothness of the L1-norm, as well as the non-linear function q, make solving problem 4 challenging, a variable splitting (Wang *et al* 2008, Bano *et al* 2020, Corona *et al* 2021, Hufnagel *et al* 2022) approach was used: Auxiliary variables $w_t := q_t(\Gamma)$ for all t and $n := \Gamma$ were introduced, and these equalities were relaxed by including two quadratic penalty terms, weighted by α and β. This yielded equation (5):

$$\min_{\Gamma,\mathrm{w},\mathrm{n}} \sum_{s=1}^{N_S}\sum_{t=1}^{N_T} \|y_{t,s} - R\,F\,C_s\,M_{t,s}^{C}\,M_s^{B}\,A_s\,w_t\|_2^2 + k\,\|G\,\mathrm{n}\|_1 + \alpha\,||w_t - q_t(\Gamma)||_2^2 + \beta\,||n - \Gamma||_2^2. \quad (5)$$

Problem 5 was split into three subproblems, and the solution of problem 4 was approached by alternating the minimization of the subproblems. For that, only one of the variables of the subproblem was optimized, and the two others were fixed

Fixing Γ and w thus led to

$$\min_{\mathrm{n}} \beta/k\,||n - \Gamma||_2^2 + ||G\,\mathrm{n}||_1. \quad \text{(subproblem I)}$$

Subproblem subproblem I was solved using the iterative algorithm proposed in (Chambolle 2004).

Fixing Γ and n thus led to

$$\min_{\mathrm{w}} \sum_{s=1}^{N_S}\sum_{t=1}^{N_T} ||y_{t,s} - R\,F\,C_s\,M_{t,s}^{C}\,M_s^{B}\,A_s\,w_t||_2^2 + \alpha\,||w_t - q_t(\Gamma)||_2^2\,. \quad \text{(subproblem II)}$$

Subproblem subproblem II was solved using a conjugate gradient approach.

Fixing w and n and updating Γ led to

$$\min_{\Gamma} \sum_{s=1}^{N_S}\sum_{t=1}^{N_T} \alpha|||w_t| - |q_t(\Gamma)|||_2^2 + \beta||n - \Gamma||_2^2. \quad \text{(subproblem III)}$$

Since the phase difference between w_t and $q_t(\Gamma)$ was assumed not to influence the other subproblems relevantly, the constraint was further relaxed by $\angle w_t = \angle\, q_t(\Gamma)$, similarly to Caballero *et al* (2014). Subproblem subproblem III was solved using the limited-memory Broyden–Fletcher–Goldfarb–Shanno algorithm (Liu and Nocedal 1989).

To approach the solution of problem 4, all subproblems were alternated three times.

For initialization of Γ and subproblem subproblem III, the individual slices of the LR stacks were reconstructed using a conjugate gradient approach, a three-parameter fit (Deichmann and Haase 1992, Becker *et al* 2019) was applied and combining these maps using the transpose of A resulted in Γ_0. For initialization of subproblem subproblem I, n was set to Γ_0. Subproblem subproblem II was initialized by $w_t = q_t(\Gamma_0)$. Γ_0 for initialization of the subproblems was updated after every alternation.

2.2. Super-resolution acquisition with rotated stacks

For SRR, several LR stacks are acquired, where each stack consists of multiple parallel slices. The stacks are oriented along the long axis of the heart to cover as much of the heart as possible with each stack. The stacks are centred at the septum, so the septum serves as a rotation axis for all stacks. Gaps are introduced between the slices to cover the whole heart with every stack.

Ideally, each HR position gets the same amount of information from the LR stacks. However, the gaps between the slices could lead to an inhomogeneous amount of information contribution to different HR positions: Regions where slices from different stacks overlap lead to a high amount of LR information and regions where slice gaps overlap lead to little LR information. To reduce this effect, some stacks share the same orientation as another stack but are shifted along the SE direction to fill the slice gaps.

The downsampling operator A describes the geometry between the different stacks, so the rotation and the relationship between a HR and LR slice. This relationship is based on the excitation slice profile, calculated from Bloch simulations of the radio frequency (RF) pulse (Pauly *et al* 1991, Rund *et al* 2018).

Every stack is acquired in a separate BH.

2.3. Motion estimation

The cardiac motion is estimated using the MIRTK Toolkit (Rueckert *et al* 1999) as described in Kerkering *et al* (2023). The method consists of three main steps. Firstly, dynamic images with high temporal resolution are reconstructed from the Golden radial acquisition scheme to capture cardiac motion. Subsequently, a preliminary diastolic T1 map is generated using dynamics only from the diastolic phases to minimize motion artefacts. This preliminary T1 map is of limited accuracy but sufficient to calculate synthetic dynamics that have the same T1-contrast characteristics as the reconstructed dynamics but for the diastolic phase only, i.e. without any cardiac motion. Afterwards, non-rigid motion estimation is performed between the reconstructed and synthetic dynamics to determine the cardiac motion fields. This approach ensures that image registration is consistently carried out between images with comparable contrast.

Spatial and temporal total variation regularization is applied to suppress undersampling artefacts (Block *et al* 2007). The motion estimation is accelerated by manually selecting a subject-specific rectangular region of interest (ROI) covering the whole heart. As each LR stack is acquired in a different BH, translational motion

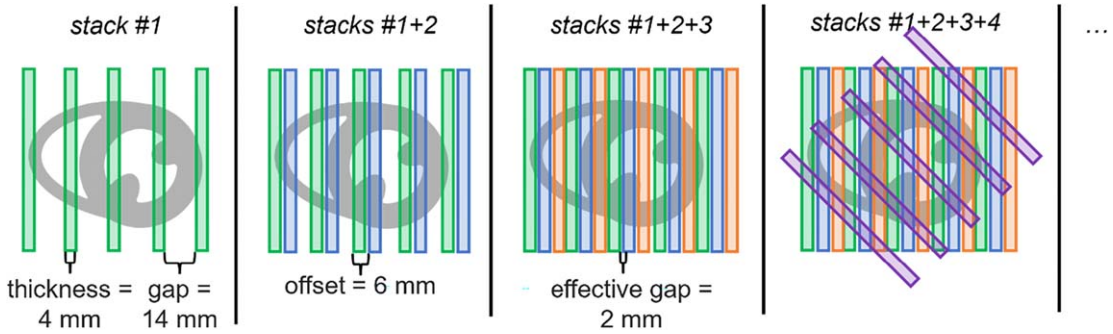

Figure 2. Schematic visualization of the planning of the first four out of 12 LR stacks. In the proposed approach, three stacks were used per orientation, shifted by 6 mm along the SE direction. This reduced the effective slice gap from 14 to 2 mm.

correction was applied to correct potential misalignments between the BH positions. For that, the LR T1 maps are interpolated onto a HR grid using A^T. All LR stacks are combined into an average stack, and every stack is registered to this average using a masked cross-correlation approach (Padfield 2012). Three iterations are used in total, resulting in M^B.

2.4. Experiments

2.4.1. General

For the data acquisition, a 3 Tesla MRI (Verio, Siemens Healthineers, Erlangen, Germany) with a 32-channel cardiac coil was used. A non-commercial 2D radial sequence was used and the slices were continuously acquired using a Golden radial scheme with an acquisition time of 2.8 s per slice. This acquisition scheme allows for retrospective image reconstruction with different temporal and spatial resolutions. One inversion pulse per slice was applied before data acquisition to make the sequence T1 sensitive. The inversion pulses were slice-selective to avoid interference between slices. The following imaging parameters were used: flip angle: 9°, TE/TR = 2.19/5 ms, 456 radial spokes per slice, field of view (FOV): 320 × 320 mm^2. For each slice, the spokes were equidistantly split into 27 dynamics with effective inversion times between 97.50 ms and 2165.00 ms. This corresponded to an undersampling factor of approximately 14.5 per dynamic. A temporal resolution of 61.40 ms was used for the cardiac motion estimation. The inversion times were the same for all LR stacks.

For SRR, 12 LR stacks consisting of five parallel slices each were acquired with an anisotropic resolution of 1.3 × 1.3 × 4.0 mm^3 and a slice gap of 14 mm. Using the proposed SRR scheme, these were reconstructed to a HR volume with isotropic 1.3 mm resolution. Every stack was acquired in an approximately 14 s BH, resulting in a total acquisition time of 2.8 min, excluding waiting times between BH. The stacks had the same positions but were rotated (0°, 45°, 90°, 135°) around the common PE axis. The septum was aligned parallel to PE, so the stacks were rotated from a 4CH to a 2CH and back to a 4CH orientation. Three stacks always shared the same orientation and were shifted by 6 mm to one another to fill the slice gaps, reducing the effective slice gap from 14 to 2 mm, as also shown in figure 2.

The presented approach was compared to a previously presented one (Hufnagel *et al* 2022), with shifted SAX stacks. For that, 12 stacks in SAX were acquired, shifted to one another by 1.5 mm along the SE direction. The overall scan time, number, and duration of BH between this reference method and the proposed approach were identical.

As nomenclature, the HR SRR result will in the following be denoted by *SRR* and a LR map by *LR*. The subscript then describes the geometry of the SRR acquisition (*rot* for rotated or *transl* for translated (Hufnagel *et al* 2022)), and the superscript the type of SRR reconstruction (*i* for image-space based (Hufnagel *et al* 2022) or *k* for k-space-based). So, the proposed method yielded SRR^k_{rot}.

For retrospective cardiac motion estimation, an ECG signal was recorded during the acquisition. The proposed cardiac motion correction scheme was used for both the image-space-based and k-space-based results.

2.4.2. Simulation

The XCAT (Segars *et al* 2010) phantom was used for simulations. Data acquisition with the same parameters as the acquisitions described above was simulated and k-space data was generated. This allowed a reconstruction analogously to the phantom or *in vivo* data, while also the ground truth HR T1 map was available. Zero-mean noise was added to the k-space data. Cardiac motion was simulated using the default XCAT settings, and different BH positions were simulated by translational shifts in the range of (10.4, 5.2, 10.4) mm. This range

refers to the HR coordinate system, with the first number indicating the long-axis direction of the myocardium and the two others indicating the short-axis directions. The simulated motion range was assumed to be half of the amplitude motion between end-expiration and end-inspiration, as reported by Scott *et al* (2009).

As SRR strongly depends on the performance of the moco (Van Reeth *et al* 2012), two different types of simulations were carried out: once only cardiac motion was simulated and corrected, but no BH motion was simulated, and once no cardiac but BH motion was simulated.

2.4.3. Phantom

The T1MES phantom (Captur *et al* 2016) was used for phantom measurements, consisting of nine tubes with T1 times for different myocardial tissues and blood.

As a reference, a scan ref_{orth} orthogonal to the axis of rotation of SRR_{rot} was acquired. So, the high in-plane resolution of ref_{orth} was in the plane to which all LR stacks were orthogonal. Therefore, the SE direction of ref_{orth} was parallel to the rotation axis of SRR_{rot}. For this, the same sequence parameters were used as described in section 2.5.1.

As a quantitative reference, an inversion recovery spin-echo reference ref_{SE} was acquired, with the same orientation as ref_{orth} and with seven inversion times between 25 and 4800 ms (TE/TR: 12/8000 ms, FOV: 143×160 mm^2, spatial resolution: $0.8 \times 0.8 \times 5$ mm^3).

2.4.4. In vivo

To evaluate the proposed approach *in vivo*, data was obtained from ten healthy subjects (7 males, and 3 females, aged 30.3 ± 2.28 years). All subjects gave written informed consent before participation, in accordance with the institution's ethical committee.

For quantitative reference, a 3(3)3(3)5 modified Look–Locker inversion recovery (MOLLI) scan was acquired with the following scan parameter: FOV: 360×323 mm^2, TE/TR: 1.12/2.7 ms, flip angle: 35°, and spatial resolution: $2.1 \times 1.4 \times 6$ mm^3. Overall, eight slices were acquired with the following orientations and positions: 4CH, 2CH of the left ventricle, 2CH of the right ventricle, and SAX at the following positions: apex, apical, mid-ventricular, basal, and atrial.

For anatomic reference, a turbo-spin-echo dark blood (TSE) sequence was used with the following parameters: FOV: 340×276 mm^2, TE/TR: 28.0/700.0 ms, flip angle: 180°, and spatial resolution: $1.3 \times 1.3 \times 5$ mm^3. Overall, five slices were acquired with the following orientations and positions: 4CH, 2CH of the left ventricle, 2CH of the right ventricle, and SAX at mid-ventricular and atrial positions.

2.5. Evaluation

2.5.1. Simulation

The results using simulated data without any simulated BH motion were evaluated by a qualitative comparison of the T1 maps to the ground truth. To assess the effect of the k-space-based reconstruction quantitatively, the edge sharpness of the septum in the T1 maps in SRR^i_{rot} and SRR^k_{rot} was calculated as described in Hufnagel *et al* (2022), which is based on the method described in Etienne *et al* (2002).

The performance of the BH alignment was evaluated by calculating the root-mean-squared error (RMSE) to the known simulated motion in mm. The reduction in RMSE compared to the maximum possible RMSE was calculated as the mean RMSE over the three spatial directions. For that, the simulated dataset with no cardiac motion was used as the performance of the cardiac moco could influence the performance of the BH moco.

2.5.2. Phantom

The edge sharpness of the phantom tubes was calculated and compared between the different approaches. The difference between the average edge sharpness of SRR^i_{rot} and of SRR^k_{rot} was evaluated on statistical difference using a paired student T-test.

Multiple ROI were set in each of the nine phantom tubes to determine the average and standard deviation (SD) of the T1 values and to compare them between SRR^i_{rot} and ref_{SE} as well as between SRR^k_{rot} and ref_{SE}. To assess the accuracy of the SRR, Pearson's correlation coefficients R^2 , the paired student T-test P-values, and the RMSE between SRR^i_{rot} and ref_{SE}, and between SRR^k_{rot} and ref_{SE} were calculated. Furthermore, a Bland–Altman plot (Bland and Altman 1999) was used to visualize the differences in the average T1 values between SRR^k_{rot} and ref_{SE}.

2.5.3. In vivo

To assess the performance of the k-space-based reconstruction in *in vivo* experiments, the T1 maps of LR_{rot}, SRR^i_{rot} and SRR^k_{rot} were qualitatively compared. Next to that, a qualitative comparison between SRR^k_{rot} and the MOLLI and TSE reference scans was performed.

For quantitative evaluation of the T1 values of the proposed approach, bull's eye plots (Cerqueira *et al* 2002) of the proposed and of the MOLLI reference scans were created and then compared. These plots follow the American Heart Association's standard 17-segment model of the left ventricle. For that, a basal, mid-cavity, apical and apex slice were selected. In the respective slices, the left ventricle was manually delineated into 17 segments in total, based on anatomic landmarks. For each segment, the mean and SD of the T1 values inside the segment were calculated.

The mean T1 values in each myocardial segment of each volunteer were calculated, and the mean and SD over the volunteers of these values were plotted for the proposed approach and the MOLLI reference. Next to that, the mean absolute difference in the segmental T1 values between the MOLLI reference and the proposed approach was calculated. The precision of the T1 values was evaluated by comparing the SD of the T1 values within the different myocardial segments between SRR and MOLLI over all segments and all ten healthy volunteers.

Improvements compared to previously published methods, as well as the impact of motion on the SRR, were investigated in a qualitative comparison between the T1 maps of SRR^{k}_{rot} and SRR^{i}_{transl}.

The influence of the k-space-based reconstruction on noise and image contrast was evaluated using the contrast-to-noise ratio CNR_{T1} of the T1 maps. This was evaluated at the septum in a 2D slice using the following equation:

$$\mathrm{CNR}_{T1} = \frac{\mu_{\mathrm{septum}} - \mu_{\mathrm{blood}}}{\sigma_{\mathrm{blood}}}. \tag{6}$$

Thereby μ_{septum} describes the mean T1 intensity in a ROI placed in the septum. μ_{blood} describes the mean T1 intensity in a ROI placed in the blood adjacent to the septum. σ_{blood} describes the SD of the T1 intensity in a ROI placed in the blood.

3. Results

3.1. Simulation

Figure 3 shows the application of the proposed approach on simulated data and compares SRR^{i}_{transl}, SRR^{i}_{rot}, SRR^{k}_{rot} and the ground truth. With the same number of LR stacks, both $\mathrm{SRR}_{\mathrm{rot}}$ approaches could cover the whole heart, while $\mathrm{SRR}_{\mathrm{transl}}$ was limited to the ventricles. The k-space-based reconstruction in SRR^{k}_{rot} improved the visualization of thin structures compared to the image-space-based reconstruction, such as, for example, the atrial wall (green arrow).

The edge sharpness of the septum was 0.28 in SRR^{i}_{rot} and 0.29 in SRR^{k}_{rot}. So, the k-space-based reconstruction increased the edge sharpness of the septum by 6.2% compared to the image-space-based reconstruction.

As evaluated in a further experiment considering different BH positions, the RMSE to the known simulated BH motion in $\mathrm{SRR}_{\mathrm{rot}}$ was [1.79, 1.59, 1.18] mm for the three different spatial directions. The maximum possible RMSE based on the simulated motion was [2.14, 2.24, 1.29] mm and thus decreased by an average of 36.83% over the three directions.

3.2. Phantom

Figure 4 shows the application of the proposed approach on phantom data and compares it with one of the LR stacks, with SRR^{i}_{rot} and with ref_{orth}. The sharpness of all tubes increased from 0.33 ± 0.05 for SRR^{i}_{rot} to 0.35 ± 0.05 for the proposed reconstruction SRR^{k}_{rot}. This corresponded to an increase in the sharpness of the tubes by 4.73% through the k-space-based reconstruction. The difference in sharpness values was statistically significant ($P = 0.01$). The sharpness in ref_{orth} was 0.45 ± 0.08.

The average T1 values of SRR^{k}_{rot}, SRR^{i}_{rot} and SRR^{i}_{transl} showed a high correlation ($P > 0.4$, $R^2 > 0.99$) with the spin-echo reference ref_{SE} as also shown in the Bland–Altman plot in figure 5. The mean difference between the T1 times in SRR^{i}_{transl} and ref_{SE} was 14.65 ± 19.66 ms, between SRR^{i}_{rot} and ref_{SE} 14.88 ± 22.4 ms, and between SRR^{k}_{rot} and ref_{SE} 14.70 ± 23.42 ms. This respectively corresponds to a RMSE of 24.52 ms, 26.89 ms and 27.66 ms for SRR^{i}_{transl}, SRR^{i}_{rot}, and SRR^{k}_{rot}.

3.3. In vivo

In figure 6, the application of the proposed approach on *in vivo* data is compared to the image-space-based SRR approach next to one LR stack. The whole myocardium, including the atria, could be visualized with the proposed approach. The image quality improved with the k-space-based SRR, as can be seen in the decreased overall noise and the increased contrast between myocardium and blood. The visualization of small structures, such as the atrial wall or the interatrial septum, improved (see arrows).

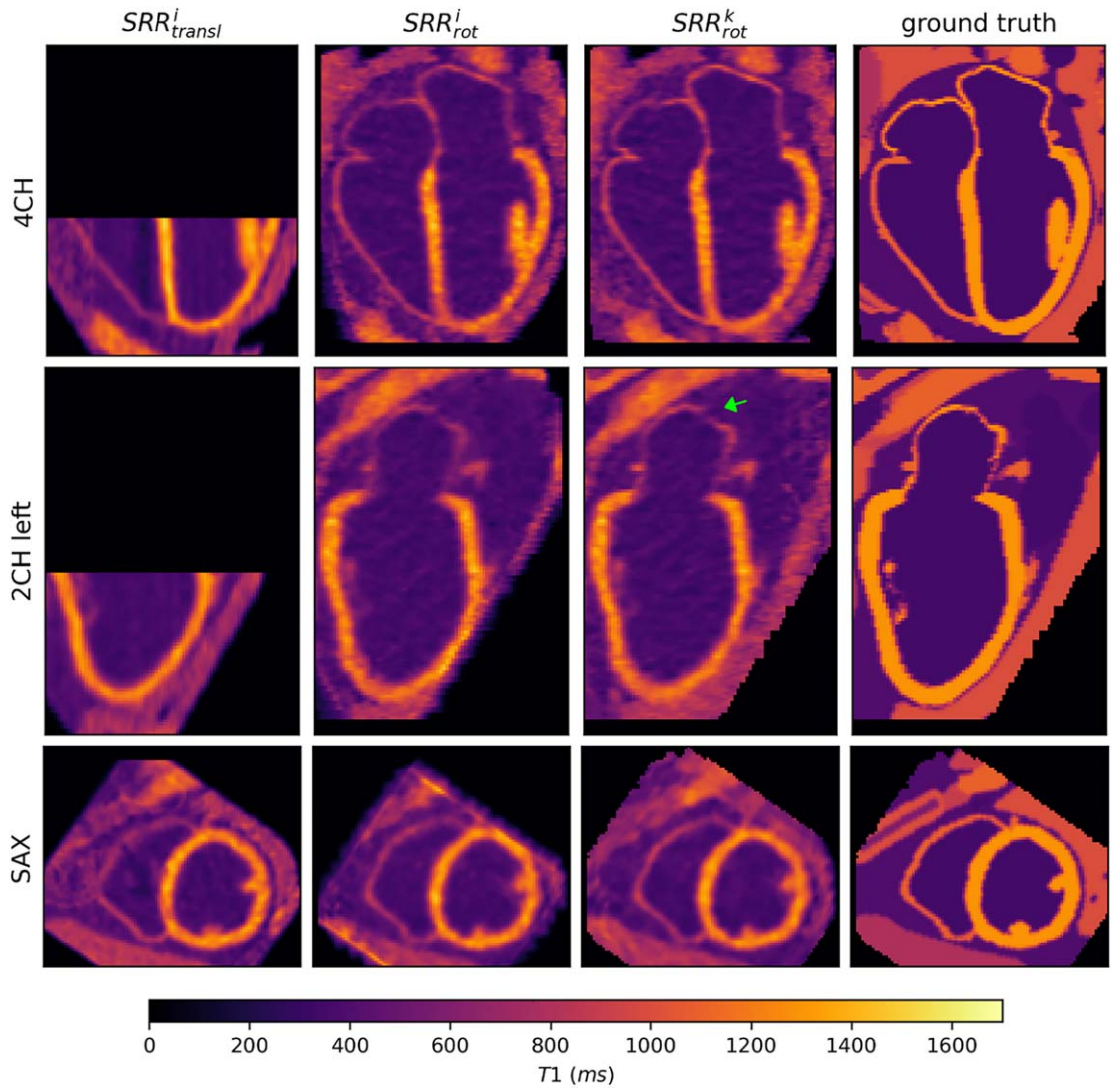

Figure 3. Application of the proposed approach on simulated T1 data. The results using a previously proposed SRR approach with translated stacks (SRR^{i}_{transl}), using image-space-based SRR with rotated stacks (SRR^{i}_{rot}) and using the proposed approach (SRR^{k}_{rot}) are compared to the ground truth. While SRR^{i}_{transl} was limited to the ventricles, the SRR_{rot} approaches could cover the whole heart with the same number of LR stacks. The use of a k-space-based reconstruction improved the visualization of small structures such as, for example, the atrial wall (arrow). Cardiac motion but no BH motion was simulated.

The CNR_{T1} of the T1 maps at the septum over all volunteers was 8.44 ± 3.30 in SRR^{i}_{rot} and 9.66 ± 3.77 in SRR^{k}_{rot}, corresponding to an increment of 14.50% using a k-space-based SRR.

Figure 7 compares SRR^{k}_{rot} of one volunteer to a MOLLI and TSE reference scan in all three orientations (SAX, 4CH, 2CH of the left ventricle). All three orientations could be captured well, and small details, such as the atrial wall (arrow), could be visualized. Additionally, figure 8 shows the results of the proposed approach applied to three more volunteers in 4CH and compares them to the reference scans. The results again matched the references and small structures as the papillary muscles could be visualized (arrow).

Figure 9 shows a bull's eye plot analysis (Caballero *et al* 2014) of the T1 times of the proposed approach and the MOLLI reference scans of all ten healthy volunteers. The mean T1 value over all volunteers and over all myocardial segments was 1068.02 ± 71.45 ms using the proposed approach and 1261.15 ± 55.50 ms using MOLLI. T1 was underestimated in the proposed approach by 193.14 ± 80.73 ms compared to MOLLI, which can be attributed to the magnetization transfer effects as a consequence of the slice-selective inversion pulses (Huang *et al* 2020, Hufnagel *et al* 2022) and residual BH motion artefacts. The SD within the myocardial segments was 64.32 ± 22.77 ms over all segments and volunteers in SRR^{k}_{rot} and 44.73 ± 31.9 ms in the MOLLI reference. These SDs were comparable, indicating high precision.

In figure 10, the proposed approach is compared to SRR^{i}_{transl}. With the same number of LR stacks, SRR^{k}_{rot} could cover the whole heart, while SRR^{i}_{transl} was restricted to the ventricles. Artefacts appearing as discontinuities in the septum (arrow) could be seen in SRR^{i}_{transl}, which could be attributed to residual motion artefacts, but not in SRR^{k}_{rot}.

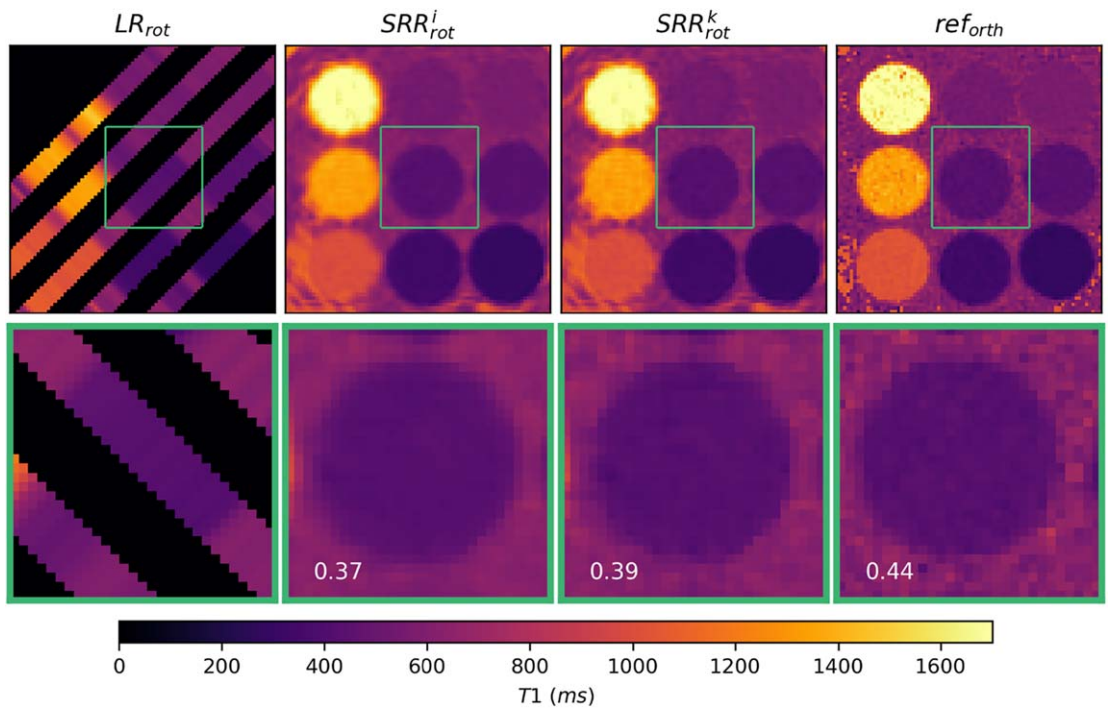

Figure 4. Application of the proposed approach on phantom T1 data. A low-resolution stack (LR_{rot}) and the outputs of image-space-based (SRR^{i}_{rot}) and k-space-based (SRR^{k}_{rot}) super-resolution reconstructions are compared to an orthogonal reference scan (ref_{orth}). The sharpness of the interface between tubes and phantom background increased when using the k-space-based SRR. This is highlighted in the zoom-ins in the second row with the measured sharpness value of the single tube in the corner.

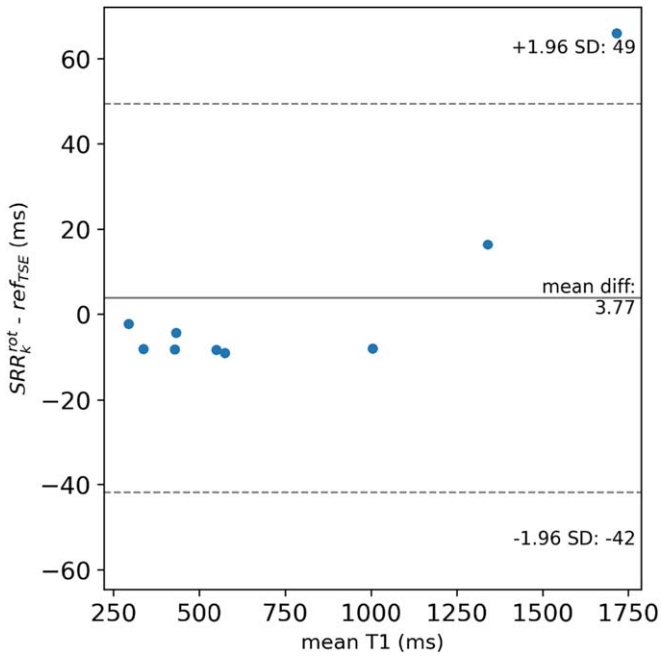

Figure 5. Bland–Altman plot between the T1 values obtained with the proposed approach SRR^{k}_{rot} and with the reference ref_{TSE}.

Figure 11 compares the application of the proposed approach to reference scans at oblique slice positions showing small myocardial structures as the SAX through the atria and the 2CH of the right ventricle. Small details in the atrial walls could be partially recovered using the proposed approach. The right ventricular wall could be fully captured.

In figure 12, the influence of motion on different SRR schemes is shown. The motion detected in SRR^{i}_{transl} was in the range of [7.8, 9.1, 2.6] mm in the three different directions and the range of [1.3, 3.9, 3.9] mm for

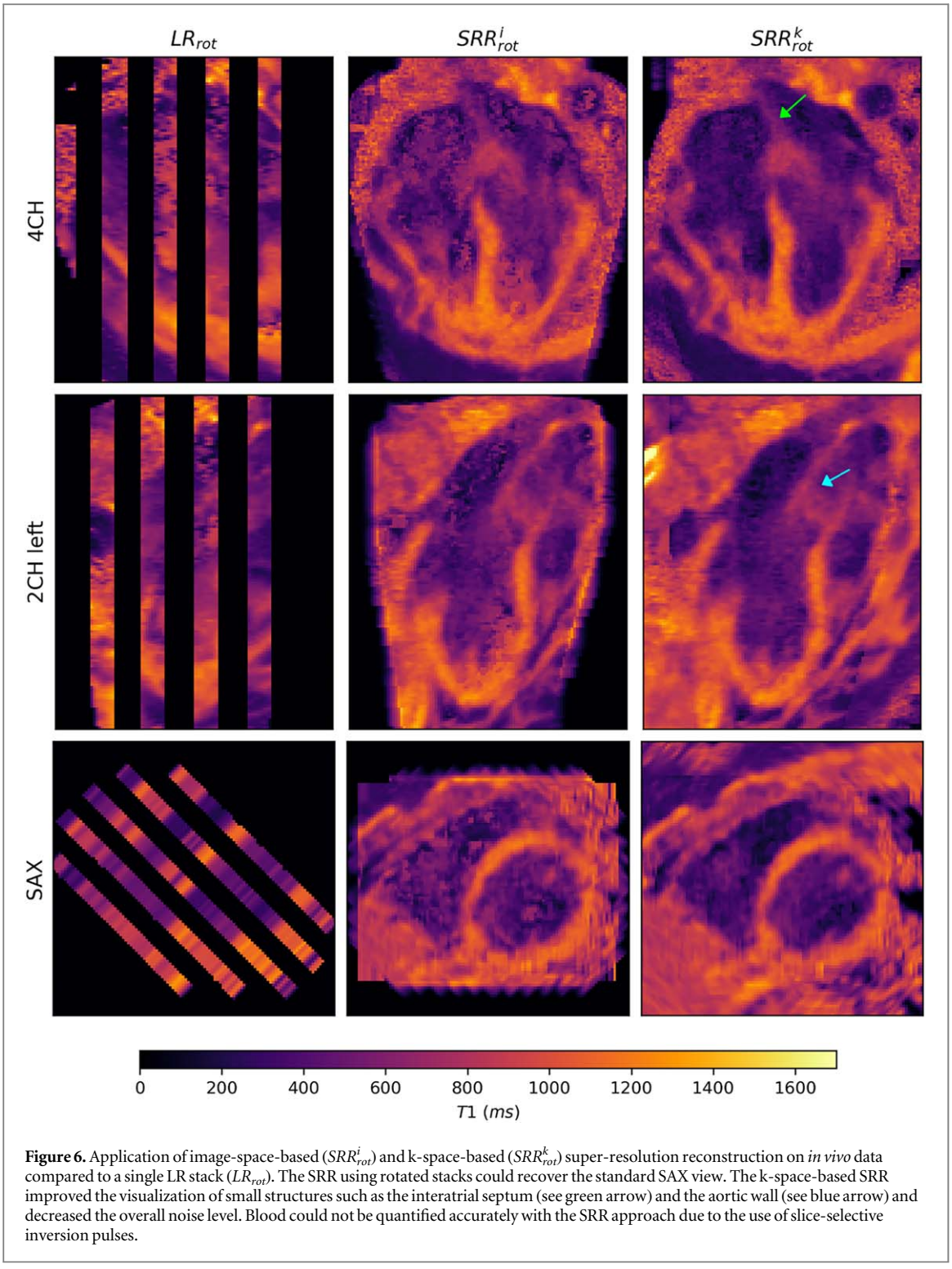

Figure 6. Application of image-space-based (SRR^{i}_{rot}) and k-space-based (SRR^{k}_{rot}) super-resolution reconstruction on *in vivo* data compared to a single LR stack (LR_{rot}). The SRR using rotated stacks could recover the standard SAX view. The k-space-based SRR improved the visualization of small structures such as the interatrial septum (see green arrow) and the aortic wall (see blue arrow) and decreased the overall noise level. Blood could not be quantified accurately with the SRR approach due to the use of slice-selective inversion pulses.

SRR^{k}_{rot}. Motion induced by different BH positions led to major zig-zag artefacts in SRR^{i}_{transl}. In the proposed approach, motion led to minor artefacts such as blurring, which could be reduced with the proposed moco scheme.

4. Discussion

In the proposed approach, a 3D whole heart T1 map could be reconstructed in an overall scan time of approximately three minutes using 12 BH. The application of a k-space-based SRR with rotated stacks improved the visualization of small structures and allowed the visualization of, for example, the wall of the right ventricle and parts of the atrial wall. Cardiac motion was corrected using non-rigid registration, and different BH

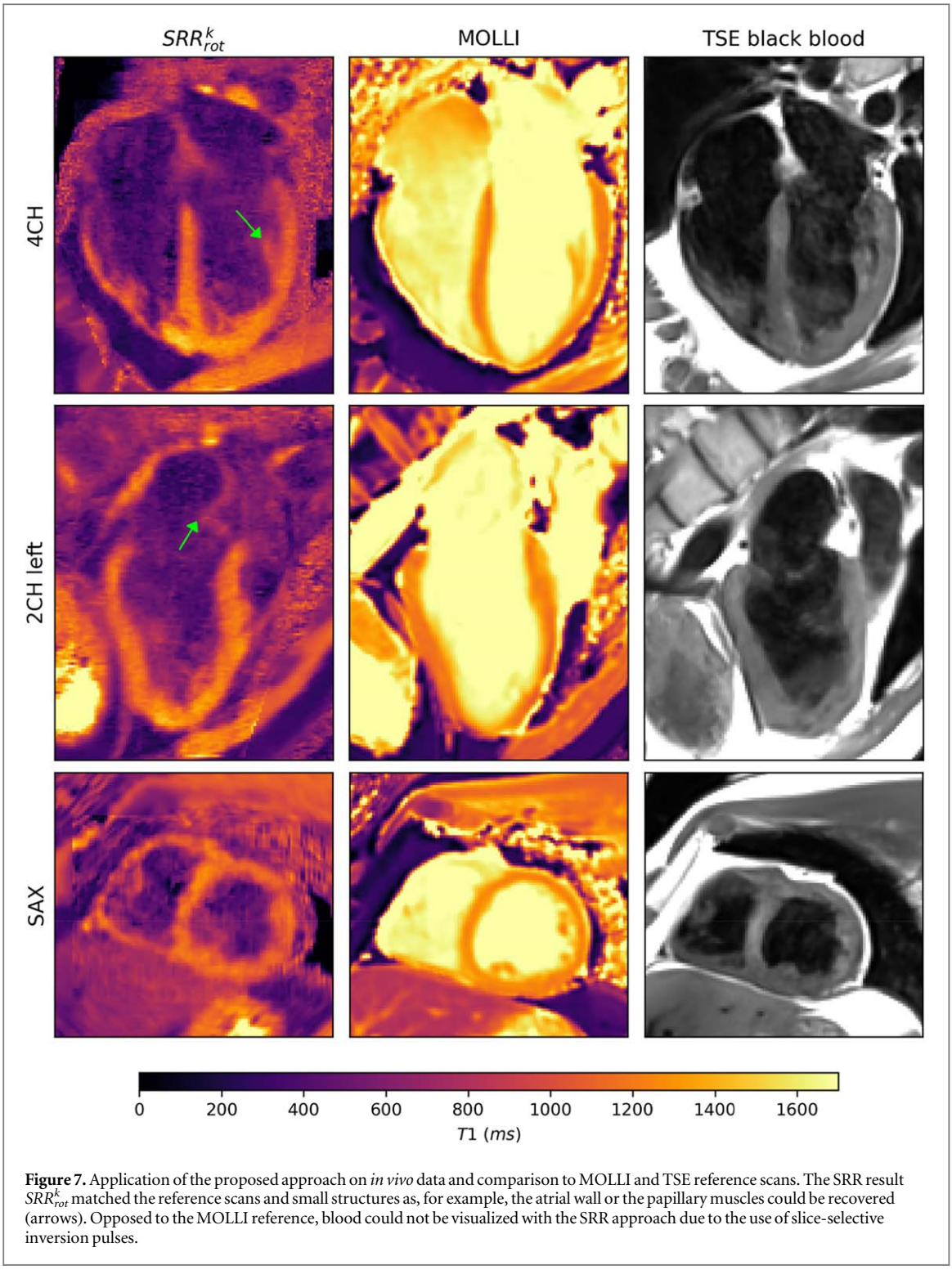

Figure 7. Application of the proposed approach on *in vivo* data and comparison to MOLLI and TSE reference scans. The SRR result SRR^{k}_{rot} matched the reference scans and small structures as, for example, the atrial wall or the papillary muscles could be recovered (arrows). Opposed to the MOLLI reference, blood could not be visualized with the SRR approach due to the use of slice-selective inversion pulses.

positions were aligned using an iterative rigid cross-correlation approach. The proposed approach provided precise T1 maps, with a comparable SD of the T1 value resulting from the proposed approach compared to the reference.

The proposed SRR approach combines multiple LR slices with high SNR to accurately measure T1 in even small structures. A similar study has demonstrated the benefits of using SRR reconstruction methods over direct HR acquisition. This study (Plenge *et al* 2012b) has shown that SRR reconstructed images have higher SNR than images obtained directly at the same high resolution when considering the same acquisition time.

The proposed k-space-based reconstruction outperformed the previously presented (Hufnagel *et al* 2022) image-space-based reconstruction. By the integration of the cardiac motion fields, the coil maps, the FT and the radial k-space trajectory into the optimization, the visualization of small structures, for example, the interatrial septum, improved, which is in accordance with previous methods proposed for SRR of the brain (Bano *et al*

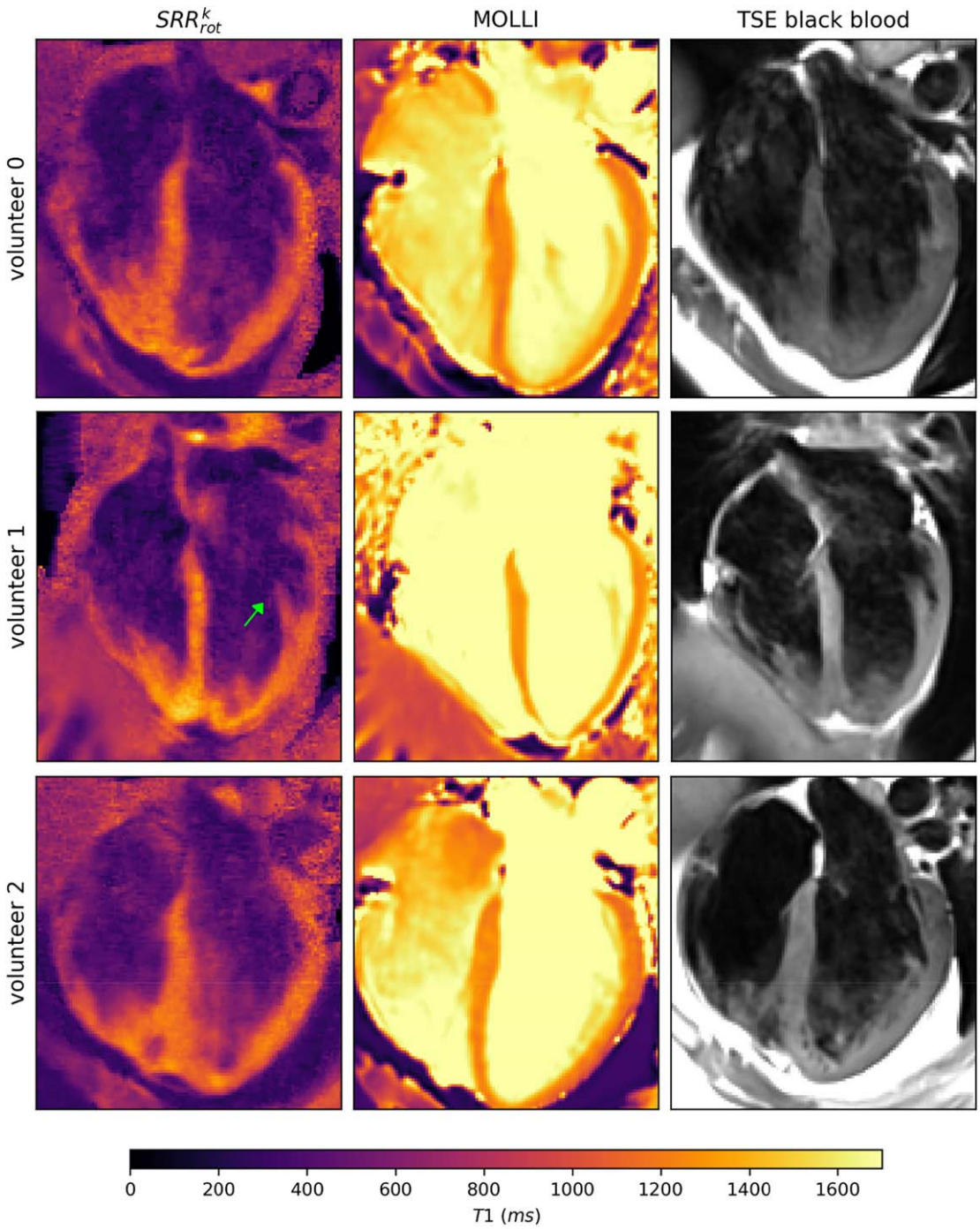

Figure 8. Application of the proposed approach on *in vivo* data and comparison to MOLLI and TSE reference scans in 4CH orientation. In addition to figure 7, three more volunteers are shown here. The SRR result SRR^{k}_{rot} matches the reference scans and small structures as, for example, the atrial wall or the papillary muscles could be captured. Blood could not be visualized with the SRR approach due to the use of slice-selective inversion pulses.

2020). Furthermore, the proposed k-space-based approach led to an increase in the edge sharpness of 4.73% compared to an image-space-based approach, as shown in phantom experiments. For the first time in quantitative cardiac imaging, a k-space-based SRR scheme with differently rotated LR stacks could be applied. It could be shown that it outperformed the results from a parallel stacks acquisition with shifts along the SE direction with respect to robustness against motion in between the LR stacks, which is in accordance with previously published results for the brain (Shilling *et al* 2009, Nicastro *et al* 2022). Furthermore, the whole heart could be covered with SRR using rotated stacks, while a SRR approach with parallel stacks was limited to the ventricles in the same acquisition time.

The results of the proposed approach agreed well with the reference scans. The *in vivo* results could not be directly compared with the MOLLI and dark blood reference scan because each scan was acquired in a different

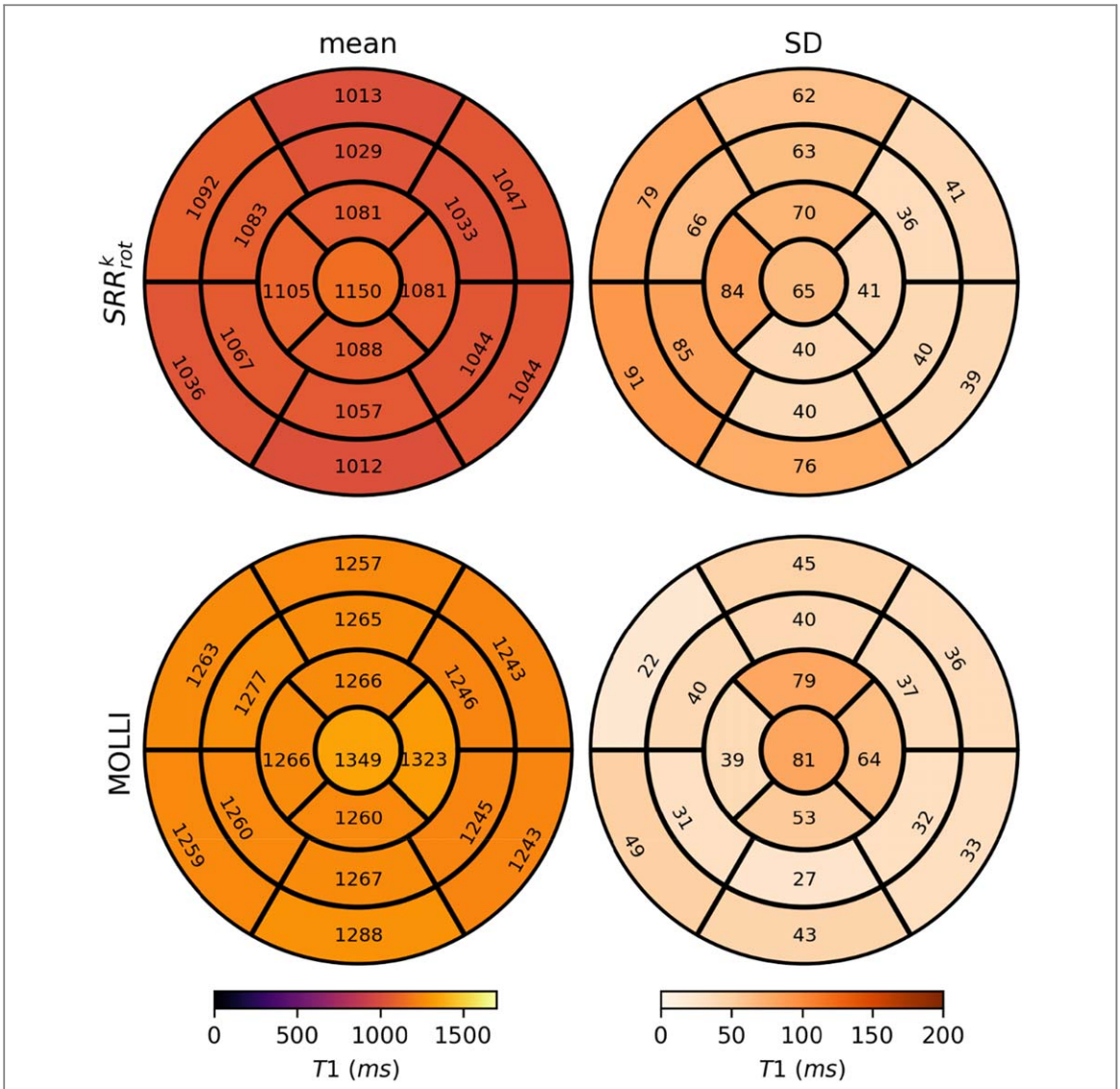

Figure 9. Bull's eye plot evaluation of the mean T1 values and their SD in ms in standardized myocardial segments of the proposed approach (SRR^{k}_{rot}) and of a MOLLI reference acquisition.

BH. Using a bull's eye plot evaluation, the *in vivo* results showed an underestimation of the myocardial T1 values compared to the MOLLI reference method. This could partly be attributed to residual motion artefacts. Nonetheless, other studies showed similar underestimation effects, which were attributed to magnetization transfer effects as a consequence of the slice-selective inversion pulses (Huang *et al* 2020, Hufnagel *et al* 2022). A similar trend of underestimation could also be shown in other studies using slice-selective inversion pulses with small animals (Kober *et al* 2004) and with healthy volunteers (Northrup *et al* 2008). The provided T1 estimates of the proposed approach, however, showed high precision. The simulations and phantom experiments suggest that the proposed approach provides accurate T1 quantification ($P > 0.61$, $R^2 > 0.99$).

Previous studies for the brain (Shilling *et al* 2009) have shown that the more stacks, i.e., orientations used for the SRR, the better the result with respect to the least mean squared error to the reference. In the proposed approach, the number of LR slices per stack and the total number of stacks were limited by BH duration and overall acquisition time. Gaps were introduced between the LR slices to cover the whole heart with every stack. To cover the heart without gaps, multiple stacks with the same orientation but shifted to each other along the SE direction were used to fill the slice gaps. These stacks could then not be used to gather information about another orientation. So, in the proposed approach, a trade-off between filling gaps and number of orientations needed to be found. The proposed approach aimed for a high homogeneity in the amount of LR information per HR position by using three stacks for each orientation.

The SRR acquisition scheme with rotated stacks leads to a higher amount of LR information per HR position the closer the HR position is to the rotation axis since more stacks overlap in this region. This can also be seen in figure 4, in which the tubes in the corner of the phantom received less LR information than the centre tube. This

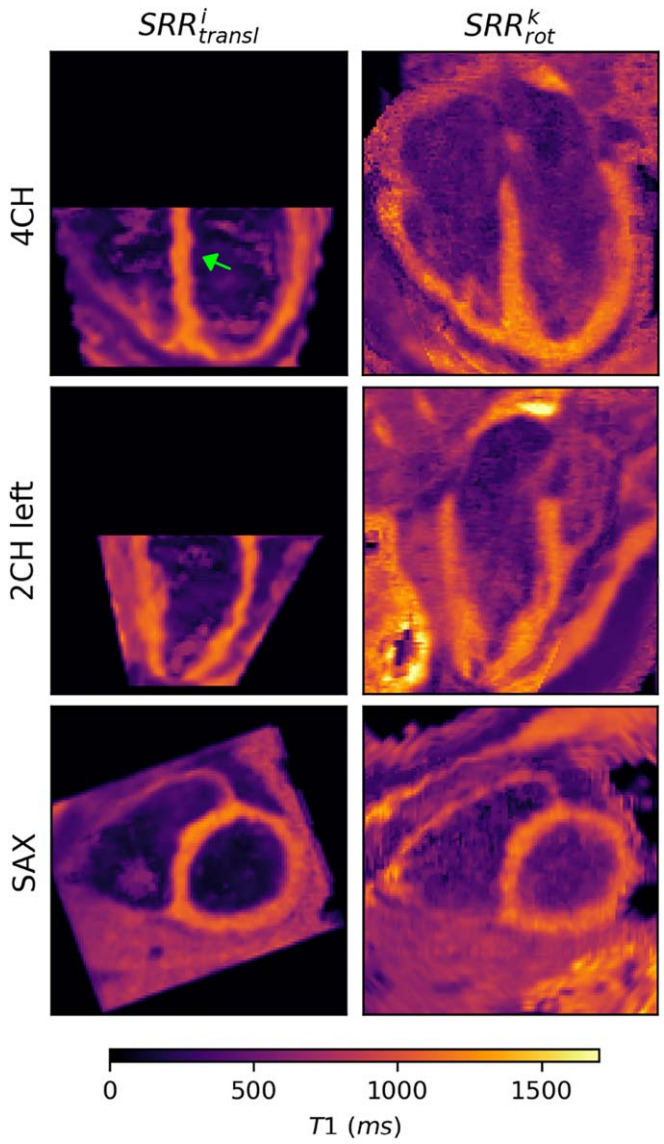

Figure 10. Comparison of the proposed approach (SRR^{k}_{rot}) to a previously presented (Hufnagel *et al* 2022) one (SRR^{i}_{transl}). With SRR^{k}_{rot}, the whole heart could be covered, while SRR^{i}_{transl} was restricted to the ventricles. Artefacts appearing as discontinuities in the septum (arrow) could be seen in SRR^{i}_{transl} but not in SRR^{k}_{rot}, which could be attributed to residual motion artefacts.

effect can be adjusted by changing the FOV in the SE direction acquired with each LR stack. The higher the covered FOV per LR stack, the farther the area with less LR information is from the rotation axis. In the proposed approach, the number of slices per LR stack was limited due to the BH duration, so the gap between the slices was adjusted such that every stack covered a FOV of 76 mm in the SE direction. This resulted in an area of maximum LR information about approximately 76 mm in diameter, centred on the septum as the axis of rotation. However, this is only sufficient for patients with a relatively small overall heart size (Pfaffenberger *et al* 2013). This can be adapted to a larger heart by increasing the gap between the slices and thus requiring more stacks to fill the gaps.

As shown in figure 12, SRR_{rot} showed less pronounced artefacts due to motion compared to SRR_{transl}, which agreed with (Nicastro *et al* 2022). Motion in SRR_{transl} led to strong zig-zag artefacts, while motion in SRR_{rot} led to minor artefacts such as blurring. Any residual uncorrected motion, therefore, also impairs the quality of the T1 maps more inSRR_{transl} than SRR_{rot}.

The proposed approach was limited by not being able to accurately quantify the T1 values of blood due to the use of slice-selective inversion pulses. However, the low apparent T1 time of blood can also be an advantage, as the contrast between the myocardium and the blood increased. This can be especially of interest for assessing small structures such as the atrial wall. To calculate the extracellular volume, the acquisition of a single LR slice with a global inversion pulse would provide the required information regarding the T1 values of the blood pool.

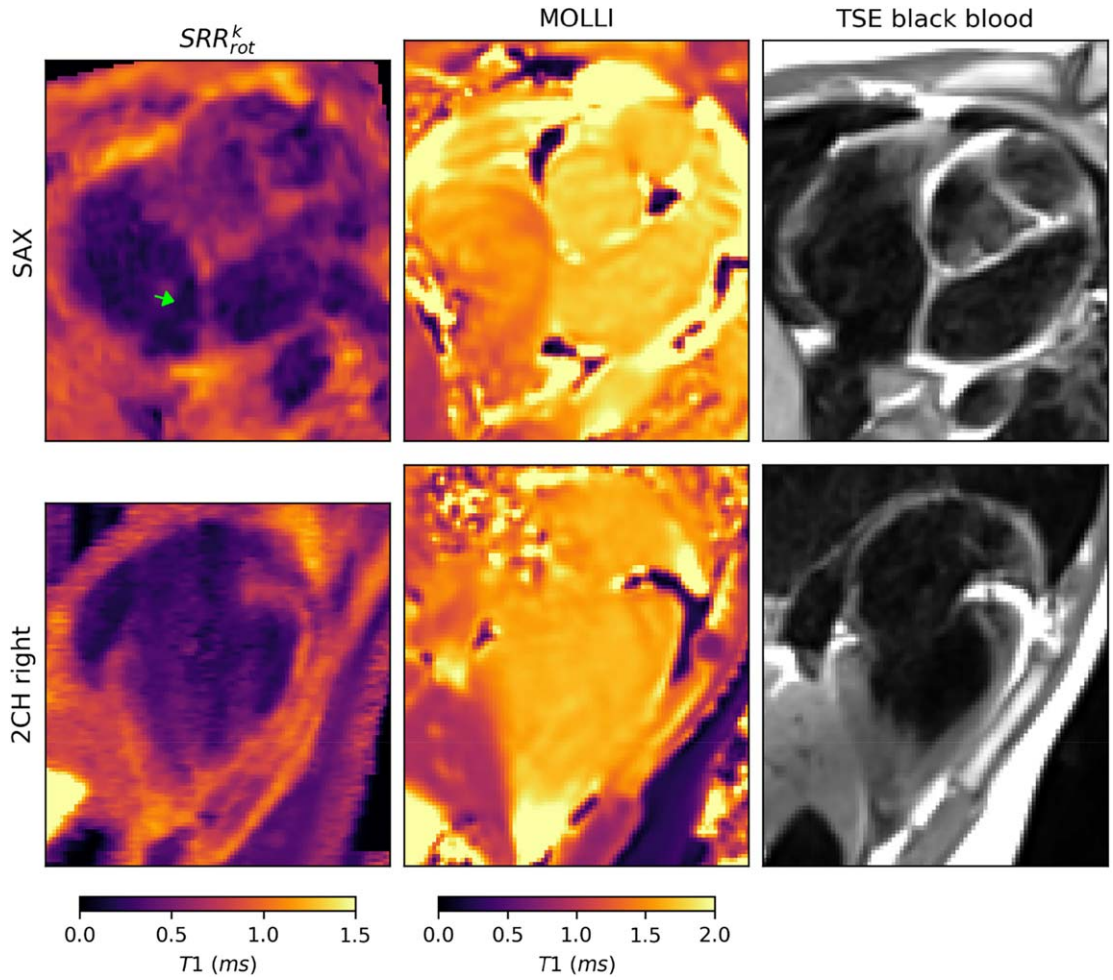

Figure 11. Application of the proposed approach (SRR^{k}_{rot}) on *in vivo* data in uncommon slice positions showing small myocardial structures and comparison to MOLLI and TSE reference scans. Small structures in the SAX view through the interatrial septum (arrow) and in the two-chamber view (2CH) of the right ventricle could be recovered with the proposed approach. Blood could not be visualized with the SRR approach due to the use of slice-selective inversion pulses. Different colour bars have been used for MOLLI and SRR^{k}_{rot} to adapt to the different T1 intensities of blood.

The use of the slice-selective inversion pulse furthermore led to a mixing of blood, which was affected by the inversion pulse and inflowing blood, which was not affected. The ejection fraction is normally below 72% for men and 74% for women (Lang *et al* 2015), so the blood that has seen the slice-selective inversion pulse at some point during the acquisition mixed with blood which has not been inverted. Especially blood in the apical region does not necessarily get ejected, so this effect is mainly visible there. The T1 value of partially inverted blood could be close to the one of a healthy myocardium, making it challenging to distinguish myocardium from blood in this region. A similar effect could be seen in the apical region of the TSE sequence. This effect would need further consideration and adaptation to use the proposed approach in patients with low ejection fraction.

A drawback of the proposed approach is the high complexity, leading to a reconstruction time of overall approximately 24 h for a HR 3D T1 map using a high-performance computer (2 × 24 Cores, Dual Intel Xeon Gold 6246, 768GB RAM). This could be improved using a physics-informed neural network instead of the alternating optimization scheme.

Another limitation of the proposed approach is that the SAX for some volunteers showed more artefacts compared to SRR_{transl}. This can be traced back to imperfectness in moco, as unknown motion between the LR stack worsens the SRR result (Van Reeth *et al* 2012). In the proposed approach, the SAX has never been acquired directly but was only reconstructed from other orientations using SRR, whereas SRR_{transl} always acquired SAX images and then reconstructed 4CH or 2CH orientations out of the SRR result. Improvements in cardiac and BH moco and using more complex motion registration algorithms (Shuzhou *et al* 2007, Kuklisova-Murgasova *et al* 2012, Kainz *et al* 2015, Amerom *et al* 2019, Beirinckx *et al* 2020, 2022, Shi *et al* 2023) might, therefore, improve the overall SRR result. The integration of the moco into the optimization scheme of the SRR, as explained in (Dzyubachyk *et al* 2015, Corona *et al* 2021, Beirinckx *et al* 2020, 2022), could enhance its results. Moreover, incorporating rotation and deformation into the moco could potentially enhance the alignment of BH states.

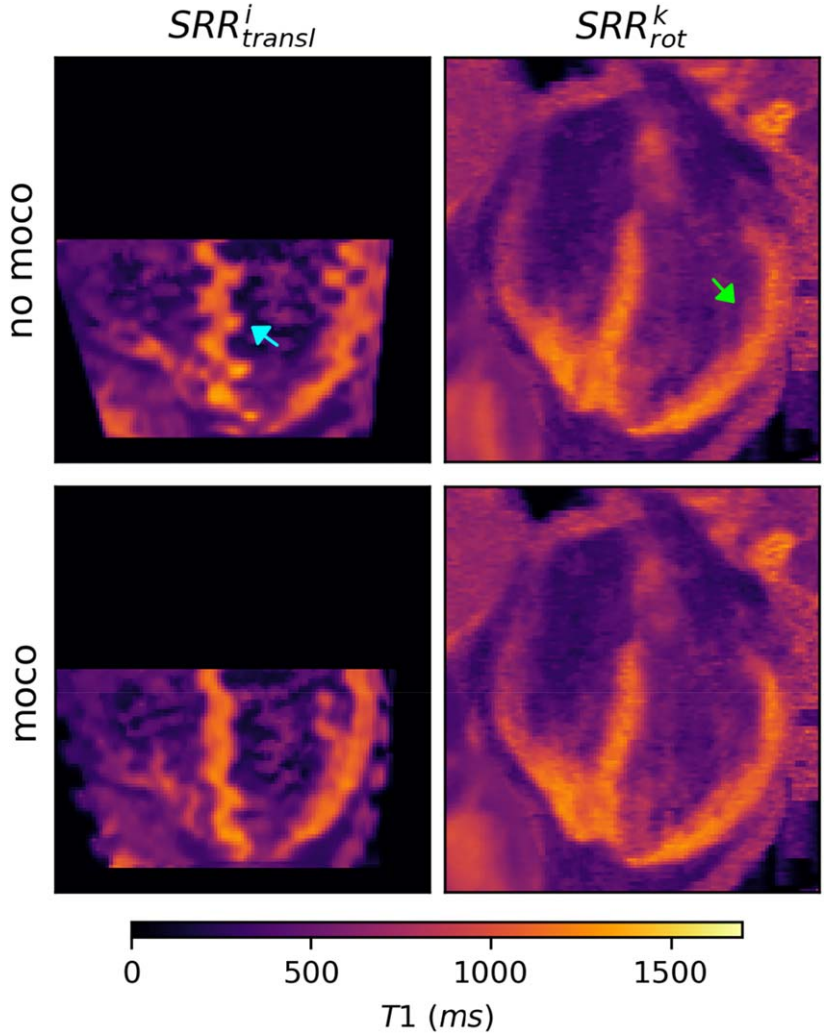

Figure 12. Comparison of the influence of motion on different SRR schemes applied to *in vivo* data. Major motion artefacts (blue arrow) were induced by different BH positions when using SRR^{i}_{transl} without any motion correction (moco). In the proposed approach (SRR^{k}_{rot}), motion between the stacks led to minor artefacts such as blurring (green arrow), which could be removed after applying the proposed moco scheme. Blood could not be visualized with the SRR approach due to the use of slice-selective inversion pulses.

This work was only evaluated in healthy volunteers. However, the application in patients might lead to further potential challenges. In this work, constant breath holds were assumed and only motion in between breath holds was corrected. Nonetheless, the application in patients could also lead to intra-stack motion, due to inadequate breath holding. This could be addressed by registering the slices within one stack individually to the HR volume. Furthermore, instead of retrospectively aligning the BH position, external respiratory motion correction approaches could be used to track the slice positions prospectively and adjust the acquisition accordingly, for instance, using the Pilot tone (Ludwig *et al* 2021). This would allow for a free-breathing acquisition and thereby increase the overall patient comfort. Furthermore, patients might show irregular heartbeats. The proposed cardiac motion correction scheme has so far not been applied to patient data. However, due to its retrospective application, it is in general independent of the heart rate and thus also independent of successful real-time triggering.

The proposed SRR reconstruction problem sets up a relationship between the acquired k-space data and the HR T1 parameter map. This formulation is versatile and can be used for various quantitative imaging techniques, including T2 mapping. The low through-plane resolution in cardiac T2 maps may limit the ability to detect small areas of inflammation (O'Brien *et al* 2022) or edema (Bustin *et al* 2021). Additionally, in cardiac T2 mapping, the FOV is often restricted to only a part of the left ventricle, potentially causing the omission of focal areas of inflammation (Bustin *et al* 2021). In the future, applying SRR to T2 mapping could also provide valuable diagnostic information related to edema (Messroghli *et al* 2017) in patients with conditions such as myocardial infarction (Giri *et al* 2009, van Heeswijk *et al* 2015), heart transplant rejection (Markl *et al* 2013), or inflammatory cardiomyopathy (Thavendiranathan *et al* 2012).

5. Conclusion

In this study, a novel 3D k-space-based super-resolution T1 mapping approach with rotated stacks was proposed. Whole heart isotropic 1.3 mm T1 maps could be acquired in an overall acquisition time of approximately three minutes. Cardiac motion and different motion states due to different breath holding were corrected. The visualization of small structures improved, and the whole heart could be covered, including the atria.

Acknowledgments

The authors gratefully acknowledge funding from the German Research Foundation for Grant Nos. 289347353 (GRK 2260, BIOQIC) and 372486779 (SFB 1340). The results presented here have been developed in the framework of the 18HLT05 QUIERO Project. This project has received funding from the EMPIR programme co-financed by the Participating States and from the European Union's Horizon 2020 research and innovation programme.

Data availability statement

The data cannot be made publicly available upon publication because the cost of preparing, depositing and hosting the data would be prohibitive within the terms of this research project. The data that support the findings of this study are available upon reasonable request from the authors.

Ethical statement

The research was approved by the institution's ethical committee ('Ethikkommission der PTB'). The research was conducted in accordance with the principles embodied in the Declaration of Helsinki and in accordance with local statutory requirements. All subjects gave written informed consent before participation. No approval ID number was specified.

ORCID iDs

Simone Hufnagel https://orcid.org/0000-0003-3942-5113
Patrick Schuenke https://orcid.org/0000-0002-3179-4830
Jeanette Schulz-Menger https://orcid.org/0000-0003-3100-1092
Tobias Schaeffter https://orcid.org/0000-0003-1310-2631
Christoph Kolbitsch https://orcid.org/0000-0002-4355-8368

References

Al-Wakeel-Marquard N *et al* 2021 Diffuse myocardial fibrosis by T1 mapping is associated with heart failure in pediatric primary dilated cardiomyopathy *Int. J. Cardiol.* **333** 219–25

Amerom J F P *et al* 2019 Fetal whole-heart 4D imaging using motion-corrected multi-planar real-time MRI *Magn. Reson. Med.* **82** mrm.27798

Asano R *et al* 2021 Prognostic value of right ventricular native T1 mapping in pulmonary arterial hypertension *PLoS One* **16** e0260456 Aimo A

Bano W *et al* 2020 Model-based super-resolution reconstruction of T2 maps *Magn. Reson. Med.* **83** 906–19

Becker K M, Schulz-Menger J, Schaeffter T and Kolbitsch C 2019 Simultaneous high-resolution cardiac T 1 mapping and cine imaging using model-based iterative image reconstruction *Magn. Reson. Med.* **81** 1080–91

Beinart R *et al* 2013 Cardiac magnetic resonance T1 mapping of left atrial myocardium *Heart Rhythm.* **10** 1325–31

Beirinckx Q *et al* 2022 Model-based super-resolution reconstruction with joint motion estimation for improved quantitative MRI parameter mapping *Comput. Med. Imaging Graph.* **100** 102071

Beirinckx Q *et al* 2020 Joint maximum likelihood estimation of motion and T1 parameters from magnetic resonance images in a super-resolution framework: a simulation study *Fundam. Inform.* ed S Brunetti *et al* vol 172, pp 105–28

Bland J M and Altman D G 1999 Measuring agreement in method comparison studies *Stat. Methods Med. Res.* **8** 135–60

Block K T, Uecker M and Frahm J 2007 Undersampled radial MRI with multiple coils. Iterative image reconstruction using a total variation constraint *Magn. Reson. Med.* **57** 1086–98

Bloomer T N *et al* 2001 Cine MRI using steady state free precession in the radial long axis orientation is a fast accurate method for obtaining volumetric data of the left ventricle *J. Magn. Reson. Imaging* **14** 685–92

Bustin A *et al* 2021 High-spatial-resolution 3D whole-heart MRI T2 mapping for assessment of myocarditis *Radiology* **298** 578–86

Caballero J, Price A N, Rueckert D and Hajnal J V 2014 Dictionary learning and time sparsity for dynamic MR data reconstruction *IEEE Trans. Med. Imaging* **33** 979–94

Captur G *et al* 2016 A medical device-grade T1 and ECV phantom for global T1 mapping quality assurance—the T1 mapping and ECV standardization in cardiovascular magnetic resonance (T1MES) program *J. Cardiovasc. Magn. Reson.* **18** w14
Cerqueira M D *et al* 2002 Standardized myocardial segmentation and nomenclature for tomographic imaging of the heart *Circulation.* **105** 539–42
Chambolle A 2004 An algorithm for total variation minimization and applications *J. Math. Imaging Vis.* **20** 89–97
Corona V, Aviles-Rivero A, Debroux N, Le Guyader C and Schönlieb C B 2021 Variational multi-task MRI reconstruction: Joint reconstruction, registration and super-resolution *Med. Image Anal.* **68** 101941
Deichmann R and Haase A 1992 Quantification of T1 values by SNAPSHOT-FLASH NMR imaging *J. Magn. Reson. (1969)* **96** 608–12
Dzyubachyk O *et al* 2015 Super-resolution reconstruction of late gadolinium-enhanced MRI for improved myocardial scar assessment *J. Magn. Reson. Imaging* **42** 160–7
Etienne A, Botnar R M, van Muiswinkel A M C, Boesiger P, Manning W J and Stuber M 2002 'Soap-bubble' visualization and quantitative analysis of 3D coronary magnetic resonance angiograms *Magn. Reson. Med.* **48** 658–66
Giri S *et al* 2009 T2 quantification for improved detection of myocardial edema *J. Cardiovasc. Magn. Reson.* **11** 56
Haaf P, Garg P, Messroghli D R, Broadbent D A, Greenwood J P and Plein S 2017 Cardiac T1 mapping and extracellular volume (ECV) in clinical practice: a comprehensive review *J. Cardiovasc. Magn. Reson.* **18** 89
van Heeswijk R B, Piccini D, Feliciano H, Hullin R, Schwitter J and Stuber M 2015 Self-navigated isotropic three-dimensional cardiac T2 mapping *Magn. Reson. Med.* **73** 1549–54
Huang L *et al* 2020 FASt single-breathhold 2D multislice myocardial T1 mapping (FAST1) at 1.5T for full left ventricular coverage in three breathholds *J. Magn. Reson. Imaging* **51** 492–504
Hufnagel S *et al* 2022 3D model-based super-resolution motion-corrected cardiac T1 mapping *Phys. Med. Biol.* **67** 245008
Jackson J I, Meyer C H, Nishimura D G and Macovski A 1991 Selection of a convolution function for Fourier inversion using gridding (computerised tomography application) *IEEE Trans. Med. Imaging* **10** 473–8
Kainz B *et al* 2015 Fast volume reconstruction from motion corrupted stacks of 2D slices *IEEE Trans. Med. Imaging* **34** 1901–13
Keiner J, Kunis S and Potts D 2009 Using NFFT 3—a software library for various nonequispaced fast fourier transforms *ACM Trans. Math. Softw.* **36** 1–30
Kerkering K M, Schulz-Menger J, Schaeffter T and Kolbitsch C 2023 Motion-corrected model-based reconstruction for ⟨scp⟩2D⟨/scp⟩ myocardial ⟨scp⟩T1⟨/scp⟩ mapping *Magn. Reson. Med.* **90** 1086–100
Kober F *et al* 2004 High-resolution myocardial perfusion mapping in small animals *in vivo* by spin-labeling gradient-echo imaging *Magn. Reson. Med.* **51** 62–7
Kuklisova-Murgasova M, Quaghebeur G, Rutherford M A, Hajnal J V and Schnabel J A 2012 Reconstruction of fetal brain MRI with intensity matching and complete outlier removal *Med. Image Anal.* **16** 1550–64
Lang R M *et al* 2015 Recommendations for cardiac chamber quantification by echocardiography in adults: an update from the american society of echocardiography and the european association of cardiovascular imaging *J.. Am. Soc. Echocardiogr.* **28** 1–39.e14
Liu D C and Nocedal J 1989 On the limited memory BFGS method for large scale optimization *Math. Program.* **45** 503–28
Look D C and Locker D R 1970 Time saving in measurement of NMR and EPR relaxation times *Rev. Sci. Instrum.* **41** 250–1
Ludwig J, Speier P, Seifert F, Schaeffter T and Kolbitsch C 2021 Pilot tone–based motion correction for prospective respiratory compensated cardiac cine MRI *Magn. Reson. Med.* **85** 2403–16
Markl M *et al* 2013 Myocardial T2-mapping and velocity mapping: changes in regional left ventricular structure and function after heart transplantation *Magn. Reson. Med.* **70** 517–26
Messroghli D R *et al* 2017 Clinical recommendations for cardiovascular magnetic resonance mapping of T1, T2, T2* and extracellular volume: a consensus statement by the society for cardiovascular magnetic resonance (SCMR) endorsed by the european association for cardiovascular imagi *J. Cardiovasc. Magn. Reson.* **19** 75
Milotta G, Bustin A, Jaubert O, Neji R, Prieto C and Botnar R M 2020 3D whole-heart isotropic-resolution motion-compensated joint T1/T2 mapping and water/fat imaging *Magn. Reson. Med.* **84** 3009–26
Nicastro M *et al* 2022 To shift or to rotate? Comparison of acquisition strategies for multi-slice super-resolution magnetic resonance imaging *Front. Neurosci.* **16** 1044510
Nordio G *et al* 2020 Whole-heart T1 mapping using a 2D fat image navigator for respiratory motion compensation *Magn. Reson. Med.* **83** 178–87
Northrup B E *et al* 2008 Resting myocardial perfusion quantification with CMR arterial spin labeling at 1.5 T and 3.0 T *J. Cardiovasc. Magn. Reson.* **10** 1–9
O'Brien A T, Gil K E, Varghese J, Simonetti O P and Zareba K M 2022 T2 mapping in myocardial disease: a comprehensive review *J. Cardiovasc. Magn. Reson.* **24** 33
Padfield D 2012 Masked object registration in the fourier domain *IEEE Trans. Image Process.* **21** 2706–18
Pauly J, Le Roux P, Nishimura D and Macovski A 1991 Parameter relations for the shinnar-le roux selective excitation pulse design algorithm (NMR imaging) *IEEE Trans. Med. Imaging* **10** 53–65
Pfaffenberger S *et al* 2013 Size matters! impact of age, sex, height, and weight on the normal heart size *Circ. Cardiovasc. Imaging* **6** 1073–9
Phair A, Cruz G, Qi H, Botnar R M and Prieto C 2023 Free-running 3D whole-heart T1 and T2 mapping and cine MRI using low-rank reconstruction with non-rigid cardiac motion correction *Magn. Reson. Med.* **89** 217–32
Plenge E *et al* 2012a Super-resolution methods in MRI: can they improve the trade-off between resolution, signal-to-noise ratio, and acquisition time? *Magn. Reson. Med.* **68** 1983–93
Plenge E *et al* 2012b Super-resolution methods in MRI: can they improve the trade-off between resolution, signal-to-noise ratio, and acquisition time? *Magn. Reson. Med.* **68** 1983–93
Qi H *et al* 2019a Free-running 3D whole heart myocardial T1 mapping with isotropic spatial resolution *Magn. Reson. Med.* **82** 1331–42
Qi H *et al* 2019b Free-running simultaneous myocardial T1/T2 mapping and cine imaging with 3D whole-heart coverage and isotropic spatial resolution *Magn. Reson. Imaging* **63** 159–69
Qi H *et al* 2020 Respiratory motion-compensated high-resolution 3D whole-heart T1ρ mapping *J. Cardiovasc. Magn. Reson.* **22** 12
Qi H *et al* 2022 Accelerated 3D free-breathing high-resolution myocardial T1ρ mapping at 3 Tesla *Magn. Reson. Med.* **88** 2520–31
Van Reeth E, Tham I W K, Tan C H and Poh C L 2012 Super-resolution in magnetic resonance imaging: a review *Concepts Magn. Reson.* A **40A** 306–25
Rueckert D, Sonoda L I, Hayes C, Hill D L G, Leach M O and Hawkes D J 1999 Nonrigid registration using free-form deformations: application to breast MR images *IEEE Trans. Med. Imaging* **18** 712–21
Rund A, Aigner C S, Kunisch K and Stollberger R 2018 Simultaneous multislice refocusing via time optimal control *Magn. Reson. Med.* **80** 1416–28

Schelbert E B and Messroghli D 2016 State of the art: clinical applications of cardiac T1 mapping *Radiology* **278** 658–76
Scott A D, Keegan J and Firmin D N 2009 Motion in cardiovascular MR imaging *Radiology* **250** 331–51
Segars W P, Sturgeon G, Mendonca S, Grimes J and Tsui B M W 2010 4D XCAT phantom for multimodality imaging research *Med. Phys.* **37** 4902–15
Shi W *et al* 2023 AFFIRM: affinity fusion-based framework for iteratively random motion correction of multi-slice fetal brain MRI *IEEE Trans. Med. Imaging* **42** 209–19
Shilling R Z, Robbie T Q, Bailloeul T, Mewes K, Mersereau R M and Brummer M E 2009 A super-resolution framework for 3D high-resolution and high-contrast imaging using 2D multislice MRI *IEEE Trans. Med. Imaging* **28** 633–44
Shuzhou J, Hui X, Glover A, Rutherford M, Rueckert D and Hajnal J V 2007 MRI of moving subjects using multislice snapshot images with volume reconstruction (SVR): application to fetal, neonatal, and adult brain studies *IEEE Trans. Med. Imaging* **26** 967–80
Van Steenkiste G *et al* 2016 Super-resolution reconstruction of diffusion parameters from diffusion-weighted images with different slice orientations *Magn. Reson. Med.* **75** 181–95
Van Steenkiste G *et al* 2017 Super-resolution T1 estimation: quantitative high resolution T1 mapping from a set of low resolution T1-weighted images with different slice orientations *Magn. Reson. Med.* **77** 1818–30
Thavendiranathan P *et al* 2012 Improved detection of myocardial involvement in acute inflammatory cardiomyopathies using T2 mapping *Circ. Cardiovasc. Imaging* **5** 102–10
Wang Y, Yang J, Yin W and Zhang Y 2008 A new alternating minimization algorithm for total variation image reconstruction *SIAM J. Imaging Sci.* **1** 248–72
Whitaker J *et al* 2016 The role of myocardial wall thickness in atrial arrhythmogenesis *Europace* **18** euw014